# EQUIATOMIC CoCrFeNi THIN FILMS ON C-SAPPHIRE: THE ROLE OF TWINS AND ORIENTATION RELATIONSHIPS

Maya K. Kini[1,2,*], Subin Lee[1,3], Alan Savan[4], Benjamin Breitbach[1], Matteo Ghidelli[1,5], Alfred Ludwig[4], Christina Scheu[1], Dominique Chatain[1,6], James P. Best[1], Gerhard Dehm[1*]

1 Max-Planck-Institut für Eisenforschung GmbH, Max-Planck-Straße 1, 40237 Düsseldorf, Germany

2 *Current Address*: School of Minerals, Metallurgical and Materials Engineering, Indian Institute of Technology Bhubaneswar, Jatni, Khorda 752050, Odisha, India

3 *Current Address*: Institute for Applied Materials, Karlsruhe Institute of Technology, Kaiserstraße 12, 76131 Karlsruhe, Germany

4 Materials Discovery and Interfaces, Institute for Materials, Ruhr University Bochum, 44780 Bochum, Germany

5 *Current Address*: Laboratoire des Sciences des Procédés et des Matériaux (LSPM), CNRS, Université Sorbonne Paris Nord, 93430, Villetaneuse, France

6 Aix-Marseille Univ, CNRS, CINAM, 13009 Marseille, France

*Corresponding authors

Email id: mayakini@iitbbs.ac.in, g.dehm@mpie.de,

**Abstract**

Face centered cubic (fcc) metals deposited onto crystalline substrates grow heteroepitaxially with specific orientation relationships (ORs). The ORs depend on a number of factors including lattice mismatch, bonding and the relative symmetry between the surface and the film. Less explored factors include defects like growth and annealing twins. In this study, we report the presence of a high density of nanotwins in as-deposited films delaying grain growth of OR1 ($\{111\}_{fcc} \parallel (0001)_{Al_2O_3}$, $\langle 110\rangle_{fcc} \parallel \langle 10\bar{1}0\rangle_{Al_2O_3}$) grains up to 0.56 $T_m$. A new OR with respect to the c-sapphire substrate is found, compared to the well-known OR1 and OR2 which grow with the $\{111\}_{fcc} \parallel (0001)_{Al_2O_3}$, but differ by a 30° in-plane rotation. The new OR is named OR3 and grows above 0.56 $T_m$ with the $\{100\}_{fcc}$ parallel to the c-plane of sapphire ($\{001\}_{fcc} \parallel (0001)_{Al_2O_3}$, $\langle 100\rangle_{fcc} \parallel \langle 10\bar{1}0\rangle_{Al_2O_3}$),. The growth of OR3 is related to strain and twin boundary energy advantage.

An unusual orientation relationship $\{345\}_{fcc} \parallel (0001)_{Al_2O_3}$ is observed in most thin films containing OR3, occupying an area fraction of > 0.3. A minute (< 0.05) but consistent fractions of $\{447\}_{fcc} \parallel (0001)_{Al_2O_3}$, $\{115\}_{fcc} \parallel (0001)_{Al_2O_3}$ and $\{221\}_{fcc} \parallel (0001)_{Al_2O_3}$ $\{236\}_{fcc} \parallel (0001)_{Al_2O_3}$, $\{146\}_{fcc} \parallel (0001)_{Al_2O_3}$ all related to the formation of annealing twins in exact and near $\{001\}_{fcc}$

and $\{111\}_{fcc}$ grains are observed. The study opens new directions in the crystallography of ORs, considering the role of twins in fcc films in addition to the well-known surface and strain energies.

**Keywords:** Thin films; orientation relationships; nanotwins; twinning; physical vapor deposition; CoCrFeNi alloy

**1. Introduction**

Face centered cubic (fcc) metals on single crystal substrates such as sapphire grow heteroepitaxially, in the absence of interdiffusion[1]. The orientation relationships (ORs) and number of orientation variants depend on a number of factors including the crystallographic symmetry of the substrate surface and the thin film material[1][2]. The most observed OR for fcc metals on a surface with a threefold rotational symmetry (such as c-sapphire $(0001)_{Al_2O_3}$ or $\{111\}_{Si}$) is the one with close packed planes and directions (of the metal and the substrate) aligned parallel to each other[3][4]. Examples for this OR (referred as OR1 where $\{111\}_{fcc} \parallel (0001)_{Al_2O_3}$ , $\langle 110\rangle_{fcc} \parallel \langle 10\bar{1}0\rangle_{Al_2O_3}$) have been observed in Al[4][5], Cu [6] , Ni[7][8], Au[9], Pt [10] and a quaternary CoCrFeNi alloy [11] all grown on c-sapphire. For most fcc metals on $\{111\}_{Si/Ge}$ a similar OR is observed [1].

Many studies for fcc metals on c-sapphire also report an alternate OR, wherein the close-packed plane normals are still aligned but crystals are rotated 30° about $[0001]_{Al_2O_3}$. This OR (termed OR2 with $\{111\}_{fcc} \parallel (0001)_{Al_2O_3}$, $\langle 110\rangle_{fcc} \parallel \langle 11\bar{2}0\rangle_{Al_2O_3}$) is observed in Cu[3][12], Al [5] and a CoCrFeNi high entropy alloy (HEA) [11]. Additional ORs are also observed in solid- and liquid-state dewetted particle systems [13], that allow more freedom for particle reorientation.

Sputter deposited thin films of fcc metals or alloys with a low stacking fault energy (SFE) deposited on amorphous surfaces exhibit a high density of growth defects like stacking faults and twins[14]–[18]. The twins grow with a few nanometers spacing, especially in $\{111\}_{fcc}$ textured grains. Nanotwins, among other defects, are determining factors for microstructural stability [14] and transformation from $\{111\}_{fcc}$ to $\{001\}_{fcc}$ fiber texture with increasing film thickness[19].

In this paper, texture and heteroepitaxy in thin film fcc equiatomic CoCrFeNi alloys are studied using X-ray diffraction (XRD) and electron backscatter diffraction (EBSD) techniques. Firstly, a new heteroepitaxial relationship is reported in addition to 'OR1' and 'OR2' for fcc metallic systems on a c-sapphire substrate. Possible energetic and kinetic reasons are discussed together with the similarities and differences with pure metal/ simpler alloy systems reported in literature. Secondly, formation of extensive growth twins ('nanotwins') in this alloy, in OR 1 oriented grains is reported. Conditions for the exceptional thermal stabilities and rapid grain growth of OR1 under the influence of these twins are discussed. Theoretical considerations are accompanied with transmission electron microscopy (TEM) observations. Thirdly, influence of a surface oxide layer and a fine dispersion of oxide inclusions in the matrix on the relative grain growth of OR1, OR2 and OR3 is discussed. Fourthly, several ORs with $\{hkl\}_{fcc} \parallel (0001)_{Al_2O_3}$ where $\{hkl\}_{fcc}$ are high index, low symmetry planes falling inside the standard cubic stereographic triangle are reported. The theory behind the possible origin of these ORs due to twinning of near $\{001\}_{fcc}$ and $\{111\}_{fcc}$ orientations is proposed.

To the best of the authors knowledge, the formation of OR3 on c-sapphire is here reported for the first time (although a similar OR is reported for Al on $\{111\}_{Si}$ [20]). Also, the theoretical grounds on the consistent formation of high index $\{hkl\}_{fcc}$ ORs due to an interplay of twinning and strain energy. These findings open a new horizon for the theory of crystallography based on defects in alloy thin films, with possible implications in future studies on interconnect applications.

## 2. Experimental procedure

### 2.1. Thin film deposition

Films of CoCrFeNi alloy with thicknesses of 500 nm and 1 µm were deposited on $(0001)_{Al_2O_3}$ (c-sapphire) by magnetron co-sputtering in a load locked ultra-high vacuum chamber (CMS 600/400 LIN DCA Instruments Oy, Finland). Substrates used were 50 - 100 mm diameter c-sapphire wafers (basal plane $(0001)$ α-$Al_2O_3$, one side epi-polished, (CrysTec GmbH, Germany). All wafers were used in as-received condition with no further surface thermal or chemical treatment. Magnetron co-sputtering was carried out using confocally placed 100 mm diameter pure metal targets of Cr (99.95 wt%, MaTecK, Germany), Fe (99.99 wt%, Evochem, Germany), Co (99.99 wt%, MaTecK) and Ni (99.995 wt%, K.J. Lesker, USA). The targets were cleaned by sputtering against closed, individual target shutters prior to deposition. The base pressure of the sputter system was 4.5 x $10^{-6}$ Pa and the Ar pressure during sputtering was 0.67 Pa. Source power of the magnetrons was adjusted for each source to yield the desired equiatomic composition of the deposited film, resulting in an overall deposition rate of 0.13 nm/s. Sample stage rotation was set to 20 rpm to obtain homogeneous films. The equiatomic films were deposited at either room temperature (RT, 298 K), i.e., without intentional heating or with the heater set to 573 K. The 500 nm film on c-sapphire deposited at 298 K was annealed in the deposition chamber at 573 K for 12 hours. This film is referred to as RT deposited 500 nm film hereafter.

### 2.2 Annealing

The films on substrates were broken into 10 mm x 10 mm squares or parallelopipeds using a diamond scribe, for annealing after deposition. All 500 nm thick films grown on c-sapphire were annealed at 973, 1223 and 1373 K, while 1 µm thick films on c-sapphire were annealed at 973 and 1223 K. The holding time during annealing was 2 hours in each case. Table 1 summarizes all the investigated samples. Annealing at 973 and 1223 K were carried out in a custom-built oven with a pyrolytic BN heater operating under medium vacuum of $10^{-2}$ Pa at the annealing temperature. Annealing at 1373 K was performed at $10^{-3}$ Pa in a box type vacuum furnace.

Selected films were encapsulated individually in quartz tubes, followed by evacuation, filling with Argon and sealing. Sealed tubes also contained titanium filings as an oxygen getter. Quartz encapsulated samples were annealed at 973, 1223 K in a box type vacuum furnace.

**2.3 Characterization**

Thin films were analyzed using X-ray diffraction (XRD) in a Seifert diffractometer equipped with an ID3003 generator, poly-capillary beam optics, and a 2-circle goniometer, using $Co - K$ radiation and an energy dispersive point detector. The $\theta - 2\theta$ measurements were carried out with a step size Δ2θ of 0.03°, a count time of 10 s/step. A θ-offset of 10° was used to avoid signals from the substrate. For pole figure measurements, the diffractometer was also equipped with a 4-circle goniometer that enabled measurements with a φ range of 0 – 360° about the rotation axis and a ψ range of 0 – 85° about the tilt axis with a step size of 5° each. Pole figures were measured at 2θ values corresponding to $\{111\}$, $\{200\}$ and $\{220\}$ poles. The normal direction to the "flat" ($\{11\bar{2}0\}_{Al_2O_3}$ as per wafer terminology) of c-sapphire was always aligned along the y-axis during X-ray pole figure measurements. Scanning electron microscopy (SEM) was carried out on a high-resolution field emission gun SEM (Zeiss Gemini 500, Carl Zeiss AG, Germany). EBSD was performed using a TSL-OIM data acquisition system (Edax-Ametek, USA) attached to a Ga focused ion beam (FIB)-SEM cross beam workstation (Zeiss Auriga, Carl Zeiss AG, Germany). Oxide scale (with a thickness between 100 and 200 nm in different films) formed on annealed samples (except some quartz encapsulated samples) was removed by Ar ion surface polishing in a precision etching coating system (PECS, Gatan, USA). A beam accelerating voltage of 5 kV, milling current of 200 μA, sample rotation of 20 rpm and beam incidence angle of 10° were used for PECS. The average chemical compositions of thin films were determined using energy-dispersive X-ray spectroscopy (EDS) in a SEM (JSM 5800 LV, Tokyo, Japan) with a INCAx-act 250 EDS system (Oxford Instruments, England) using a silicon drift detector with Peltier cooling.

In-plane grain size of as-deposited films was measured with a linear intercept method using grooves at grain boundaries formed during the deposition process. Grain sizes of annealed films were calculated from grain area using grain identification maps in the TSL-OIM data analysis software. Mean grain sizes of as-deposited films (measured by linear intercept method using SEM images) and annealed films (measured using equivalent grain area in EBSD scans) along with standard deviation of the distribution are also listed in Table 1.

To find the orientation relationship with respect to the c-sapphire substrate, a small area of the film was scratched using a steel blade, to expose the substrate. EBSD scans were collected from the substrate and the film in a single experiment – without changing orientation of the sample with respect to microscope coordinate system in between the scans.

Further, TEM microstructure analysis was carried out using an aberration-corrected instrument operating at 300 kV (Titan Themis, Thermo Fisher Scientific, USA). Cross-sectional and plan-view TEM samples were fabricated using the FIB technique detailed in a previous publication[21].

## 3. Results

The major part of results is related to the heteroepitaxy of CoCrFeNi films on $(0001)$ α-$Al_2O_3$, deposited and annealed under different conditions. Sec. 3.2 and 3.3 list observations on twins and oxides respectively – that have a profound influence on the ORs.

### 3.1. Heteroepitaxial orientation relationships

Results in this section are divided into three parts. Sec. 3.1.1 reports findings on RT deposited films that contain majorly OR1 at all annealing conditions. Sec. 3.1.2 is on 573 K deposited 500 nm films and appearance of OR 3, $\{345\}_{fcc}$, $\{115\}_{fcc}$ and $\{122\}_{fcc}$. Sec. 3.1.3 on 573 K deposited 1 µm films containing a few more $\{hkl\}_{fcc}$ in addition to OR3 and $\{345\}_{fcc}$. ORs obtained with area fraction and grain size (variant spacing) are summarized in Table 1. Compositions of all deposited films (SEM-EDS) are listed in Table S1.

#### 3.1.1. The 500 nm film deposited at RT: Predominantly OR1

In RT deposited films, a heteroepitaxial OR with two orientation variants (epitaxial and epitaxial-twinned), indicated by 6 specific positions of inclined $\{111\}_{fcc}$ peaks in X-ray pole figure (Fig. 1a) was observed. The $\langle 10\bar{1}0\rangle_{Al_2O_3}$ was parallel to the x-axis indicating an OR referred to as OR1 in many studies[3]:

$$\{111\}_{fcc} \parallel (0001)_{Al_2O_3}, \langle 1\bar{1}0\rangle_{fcc} \parallel \langle 10\bar{1}0\rangle_{Al_2O_3}$$

Results are consistent with those in our previous study (for details, refer to [11]).

The OR1 grains exhibit an exceptional thermal stability on annealing. For the annealing time of 2 hours, OR1 grains are retained at 1223 K (0.71 $T_m$) (melting temperature of 1728 K[22]) except formation of some dewetting pores. Orientation spread was within 10° for 95% of these grains according to EBSD scans (Fig. 1b). The average grain size increased from 36 nm in the as-deposited condition (RT) to 780 nm at 1223 K.

At 1373 K (0.79 $T_m$) (Fig. 1c, d), the spread in OR1 (and twinned) reduced to a few degrees, the grain size increased to 8.5 µm (Table 1). New $\{447\}_{fcc} \parallel (0001)_{Al_2O_3}$ grains (purple in Fig. 1d) with an area fraction of 0.05 were observed in addition to dewetting pores.

### 3.1.2. The 500 nm films deposited at 573 K – appearance of OR 3 and $\{hkl\}_{fcc}$

Microstructure and heteroepitaxy of the 573 K deposited films were comparable to the RT deposited films, with predominantly OR1 grains (Fig. 2a). OR1 remained stable in films annealed at 973 K. In the quartz encapsulated film, all grains detectable by EBSD were of OR1 type (Fig. 2b-e, Fig. S1), majority of grains had a CI < 0.2 (Fig. S1), implying a grain size of less than 100 nm (Table 1).

Annealing at 1223 K without encapsulation led to two new significant ORs in addition to OR1 (Fig. 3) – clearly in contrast with the RT deposited films.

The first new OR was,

$$\{001\}_{fcc} \parallel (0001)_{Al_2O_3}, \langle 100\rangle_{fcc} \parallel \langle 10\bar{1}0\rangle_{Al_2O_3} \; and \; \langle 010\rangle_{fcc} \parallel \langle 11\bar{2}0\rangle_{Al_2O_3}$$

This is denoted as 'OR3' in this manuscript as OR2 is used already in literature for

$$\{111\}_{fcc} \parallel (0001)_{Al_2O_3}, \langle 110\rangle_{fcc} \parallel \langle 10\bar{1}0\rangle_{Al_2O_3}$$

The OR3 grew with three in-plane variants rotated by 120°, $\langle 001\rangle_{fcc}$ direction aligned along one of the three $\langle 10\bar{1}0\rangle_{Al_2O_3}$ directions. Orientation spread around $\{001\}_{fcc}$ was < 10° for 95% grains. Area fraction of OR3 was ~ 0.40, the grain size > 6 µm (Fig. S2), larger compared to OR1 $\{111\}_{fcc}$ grains (~1.5 µm). The second new OR was $\{345\}_{fcc} \parallel (0001)_{Al_2O_3}$, possessing an orientation spread of less than 5° (Fig. 3b, d), an average grain size of 2 µm, and an area fraction of ~ 0.38. The grains close to $\{111\}_{fcc}$ grew with a fiber texture (combination of OR1, OR2, each with twins and orientation spread, Fig. 3d), covering an area of 0.01. Annealing at a further higher temperature (1373 K) without quartz encapsulation led to a similar combination of ORs (Fig. 5, Fig. S4), with grain sizes a factor of 1.5 – 2.3 higher compared to the 1223 K films. At 1373 K the OR1 and OR2 were clearly distinguishable.

In quartz encapsulated films annealed at 1223 K, the area fraction and grain sizes of the OR1 were an order of magnitude larger (0.78 and 23 µm respectively, Fig. 4) compared to those without encapsulation. The OR3 area fraction was reduced to 0.18, grain size (5 µm) remained comparable to the film without encapsulation. The $\{345\}_{fcc} \parallel (0001)_{Al_2O_3}$ OR was not observed, instead $\{115\}_{fcc}$ and $\{122\}_{fcc}$ that were twins in $\{111\}_{fcc}$ and $\{001\}_{fcc}$ grains were observed (Fig. S3). OR 2 with an area fraction of < 0.01 was also detected.

Hence in the films deposited at 573 K,

- OR1 remains dominant in annealed films until 973 K. OR2 and OR3 appear both in films with and without encapsulation at 1223 K. OR3 is accompanied by $\{345\}_{fcc}$ grains in films without encapsulation. The $\{345\}_{fcc}$ is replaced by $\{115\}_{fcc}$ and $\{122\}_{fcc}$ in quartz encapsulated sample.
- The grain size of OR1 is strongly dependent on the oxide layer and inclusions- increasing by an order of magnitude in their absence. The grain size of OR3 does not depend significantly on oxides.

These results lead to important implications on relative stability of ORs (Sec. 4.4).

#### 3.1.3. The 1 µm film deposited at 573 K – OR 3, $\{345\}_{fcc}$ and additional $\{hkl\}_{fcc}$

The OR of the as deposited and 973 K annealed 1 µm films was predominantly OR1 (Fig. S5) with a grain size of less than 100 nm, similar to the 500 nm thick films. At 973 K, OR3 with an area fraction of 0.03 appeared.

The area fraction of OR3 increased to 0.56 in films annealed at 1223 K without encapsulation (Fig. 6a, b, Fig. S6). Less than 0.01 area fraction of OR2 (Fig. 6c,d, Fig. S6) grains, with deviations of up to 7° from the $\{111\}_{fcc}$ were observed. The $\{447\}_{fcc}$ and $\{345\}_{fcc}$, each with a spread of less than 5° (Fig. 6b) also appeared. Some of the $\{345\}_{fcc}$ oriented crystals appeared to be twins in OR3 grains (Fig. S6). The area fractions were ~ 0.35 for $\{345\}_{fcc}$, ~ 0.04 for $\{447\}_{fcc}$ and ~ 0.01 for $\{111\}_{fcc}$. A consistent but a small area fraction of~ 0.02 for grains with $\{146\}_{fcc} \parallel (0001)_{Al_2O_3}$ and ~ 0.02 with $\{236\}_{fcc} \parallel (0001)_{Al_2O_3}$ orientations (each with a spread of less than 5°) were also present. These two orientations appeared to be distinct grains although their origin could be related to twinning (Sec. 4.5).

The distribution of ORs in the film annealed at 1223 K after quartz encapsulation was qualitatively similar to the film without it (Fig. 7, Fig. S7). These films exhibited less than 0.01 of $\{111\}_{fcc}$, ~ 0.53 of OR3 and ~0.43 of $\{345\}_{fcc}$ (Fig. 7). The grain size of both OR3 and $\{345\}_{fcc}$ were a factor of 2-3 larger compared to the films without encapsulation. The $\{236\}_{fcc}$ and $\{146\}_{fcc}$ were also observed, with an area fraction of < 0.01 (Fig.S7).

Results on the 1 µm and 500 nm films deposited at 573 K are similar except:

- OR3 appears in 1 µm samples annealed at 973 K. The $\{345\}_{fcc}$appears in films both with or without encapsulation (not replaced by $\{115\}_{fcc}$ and $\{122\}_{fcc}$).
- High index $\{hkl\}_{fcc}$ orientations, $\{447\}_{fcc}$, $\{236\}_{fcc}$ and $\{146\}_{fcc}$, not observed in 500 nm thin films are consistently found in 1223 K samples with grain sizes of 10 – 20 µm, and an area fraction < 0.05.

The appearance of OR3 at lower temperature in thicker films – indicate the strain energy advantage (Sec. 4.4). Other $\{hkl\}_{fcc}$ ORs are presumably related to strain energy or plasticity due to twinning (Sec. 4.5).

### 3.2. High density of growth twins (nanotwins) in OR1 grains and nanopores at the columnar boundaries

TEM plan-view bright field images of both RT and 573 K deposited samples, (Fig. 8a) exhibited several nanopores at triple junctions. Closely spaced linear features in the cross-section (Fig. S8) were

identified as coherent twin boundaries (CTBs) and stacking faults (SFs) on $\{111\}_{fcc}$ planes by fast Fourier transformation analysis. A high density of CTBs/SFs with several nm spacing parallel to $(0001)_{Al_2O_3}$ were present in OR1 grains (Fig. S8). Twinning was not limited to the $(111)_{fcc}$ plane parallel to $(0001)_{Al_2O_3}$, but was also present in the three $\{111\}_{fcc}$ planes inclined by 70.5° to $(0001)_{Al_2O_3}$ (Fig. 8b), traces making an including angle of 120° between the pairs. CTBs were also observed in OR1 grains in annealed samples (Figs. 8c and d) but with a larger spacing. The electron diffraction pattern taken in $\langle 110 \rangle$ zone axis revealed twin reflections (Fig. 8c). In contrast, CTBs in OR3 grains were spaced several micrometers apart when present (IPF in Figs. 6, 7). Hence TEM cross-sections appeared as single crystal grains in most of the regions (Fig. 8e).

### 3.3. Oxide surface layer and oxide particles in annealed films

Films deposited at RT and 573 K had no detectable oxide layer at the surface. However, the FIB cross sections of all films annealed without quartz encapsulation had an oxide layer with a thickness of 100 - 200 nm (Eg: Figs. S8b and d). There was a high density of oxide particles embedded in the fcc matrix (Eg: Fig. S8b) [21].

The quartz encapsulated films annealed at 973 K had an oxide layer with ~ 100 nm thickness at the surface (Fig. S8). In encapsulated samples annealed at 1223 K no surface oxide was found, but a few large oxide particles (>1 μm) – rich in Cr as observed under SEM-EDS were present (Fig. S8, brief interpretation in Appendix A). The spacings of these oxides were tens of micrometers compared to tens of nm in films annealed without encapsulation[21].

Absence of oxide layer and inclusions separated by several μm, had a huge effect on the grain size and area fractions of ORs (Figs. 2,4) in 500 nm thin films. The area fraction of OR1 increases significantly at the cost of OR3 and $\{345\}_{fcc}$ in the absence of the oxide inclusions. In the 1 μm film, there is a subtle effect on the area fractions, but the grain sizes increase by a factor of 2-3.

## 4. Discussion

### 4.1. Thermal stability of OR1 grains up to 0.56 $T_m$

All the as-deposited films are predominantly OR1, both at RT and 573 K, indicating the lower energy barrier for the nucleation and growth of the OR1 grains during thin film deposition. At 973 K all identified grains in EBSD and XRD remain OR1. The grain size remains < 100 nm for 500 nm films, < 1 μm for a film thickness of 1 μm (including quartz encapsulated films). Hence, the OR1 grains exhibit an exceptional microstructural stability up to 0.56 $T_m$. The films are covered with a thin oxide layer (Fig. S8) – including the quartz encapsulated films that were Ar filled and contained a Ti getter. The

sluggish grain growth in OR1 grains in the present study was reproducible at 973 K with no exceptions (Table 1).

The grain size is less than the film thickness at 0.56 $T_m$ - much lower compared to Cu and Ni on c-sapphire annealed at lower homologous temperatures[3][8]. Pure Ni serves a good comparison due to the proximity of $T_m$, that is 1728 K for pure Ni and 1718 K for CoCrFeNi[22]. The grain sizes for 500 nm pure Ni films on c-sapphire[8], were "at least twice the film thickness" at 773 K (0.45 $T_m$).

The exceptional thermal stability (to be precise, metastability, see Sec. 4.4) could be attributed to the presence of a large number of defects: nanotwins (Fig. 8, S8) intersecting columnar boundaries, nanopores at triple junctions (Fig. 8a), a thick oxide layer on the film surface and fine oxide dispersions in the bulk.

There are a large number of kinetic factors that lead to sluggish grain growth as discussed in the following.

***Nanotwin induced reduction in intrinsic columnar boundary mobility***: In as-deposited films, columnar grain boundaries are intersected by more than a hundred coherent twin boundaries. Thermodynamically, nanotwinned grains are less stable due to a higher defect energy (Sec. 4.4). But the kinetics of the GB migration is likely to be much slower as evident in other nanotwinned fcc metals and alloys[16][17][23]. The CTBs were observed with nano spacing – even at 973 K (Fig. S8). The CTBs could also potentially explain the difference compared to pure Ni with a high SFE[24]. Ni thin films do not contain nanotwins unless deposited with specially engineered conditions like nanotwinned seed layers or under tuned deposition parameters [25]–[27].

The direct evidence of the reduction in GB mobility in the presence of CTBs requires specially designed geometries (Fig. 9). Studies on relative GB mobilities in an extensively twinned crystal bonded to a single crystal (Fig. 9b), compared to a bicrystal with a single ITB across the cross section (Fig. 9c) would be desirable.

***Zener drag due to nanopores on triple junctions*:** The columnar OR1 grains invariably enclose fine pores at triple junctions (Fig. 8a), with an area fraction of less than 0.01. These are observed up to 973 K and are likely to exert Zener drag on triple junctions[28]. Retention of nanopores over annihilation or coarsening up to 0.56 $T_m$ indicates a low rate of grain boundary and surface diffusion. (A brief explanation on nanopores is included in Appendix B).

***Influence of oxide surface layer and particles:*** is discussed in Sec. 4.3, in relation to the grain growth of all ORs.

### 4.2. Formation of OR3 in films deposited at 573 K

This study reports for the first time a new OR on any fcc metallic material on c-sapphire (section 3.1.2), with $\{001\}_{fcc} \parallel (0001)_{Al_2O_3}$.This OR forms consistently only in annealed films deposited at 573 K and not in any RT deposited film. It was the most dominant OR next to OR1 in the study. The OR3 fraction is negligible in 573 K deposited films – but drastically increases on annealing at and above 1223 K. Further, the OR is present both in films annealed with and without quartz encapsulation.

The absence of OR3 in RT deposited films, at least within the resolution limits of XRD, indicates the absence of their nuclei at this temperature. The RT deposited films most likely contain entirely OR1 nuclei. Hence the OR remains stable up to 1373 K (0.79 $T_m$). In 573 K films, OR3 and OR2 nuclei possibly form along with OR1 during deposition as shown in a schematic (Fig. 8f). Although the fraction in as-deposited films is minute and the X-Ray PFs exhibit sharp OR1 peaks, weak OR2 and OR3 signals indistinguishable from the background could be present. The OR2 and OR3 nuclei grow into large grains consuming OR1, under favorable kinetic conditions (Sec. 4.4).

### 4.3. Rapid grain growth of OR1 above a critical temperature

In RT deposited films, where OR1 remains the major OR at all annealing temperatures (Table S2), the grain size increases to greater than the film thickness at 1223 K, rapidly increasing by an order of magnitude at 1373 K. These results indicate a critical temperature above which there is rapid OR1 grain growth.

Further films deposited at 573 K, annealed with and without quartz encapsulation at 1223 K clearly indicate that the critical temperature depends on the presence of oxides. In the absence of a quartz encapsulation, the films contained fine oxide dispersion (< 100 nm), separated by tens of nm. The quartz encapsulated films contained oxide particles of sizes visible under the SEM, separated by tens of micrometers. The OR1 area fraction and grain size drastically changes in 500 nm thin films (Figs. 2 and 4) when encapsulated. The grain size increases by a factor of 15 and the area fraction increases from less than 0.1 to 0.78. Hence the OR1 grain growth is sluggish in the presence of severe oxidation, rapidly taking off in its absence. In the presence of fine oxide particles, OR1 remains stable in grain size, but gets consumed by other ORs that rapidly grow (Sec 4.4).

The results are firstly related to the mobility of columnar GBs (ITBs) with numerous intersecting CTBs being strongly dependent on the presence of oxides or other pinning points. Secondly, all films with low OR1 grain growth rate contained surface oxide, the ones with rapid grain growth did not. The oxide layer is reported to hinder diffusion creep in thin films [29], due to a lower rate of surface diffusion. The grain growth in thin films – also likely dependent on surface diffusion – could be affected in the same manner. Thirdly, the formation of a Cr-oxide layer (in some cases, up to 200 nm thick)

leads to a decrease in Cr content in the matrix [21]. A back-of the envelope calculation indicates a reduction of Cr content from 25 to 11 at% in the film matrix for the extreme case of 200 nm thick Cr-oxide forming on a 500 nm thick film. As the thickness of the oxide layer was between 100 – 200 nm, the atomic % of Cr in the matrix will be 11 – 20%. Reduction in Cr content could change the segregation profile and the relative GB mobilities. Either one or more of the above possibilities could lead to the observed OR1 grain growth behavior. Study of these individual aspects is beyond the scope of the present study.

### 4.4. Relative stabilities of OR1 compared to OR2 and OR3

The transition from $\{111\}_{fcc}$ to $\{001\}_{fcc}$ orientations is studied in detail in fiber textured films[30]–[32] – mostly considering thermodynamic factors of interfacial and strain energies. The strong $\{111\}_{fcc}$ fiber texture at lower thicknesses, is attributed to a low interfacial energy of densely packed $\{111\}_{fcc}$ surface planes [33]. The transition to $\{001\}_{fcc}$ fiber texture takes place at higher thicknesses due to a lower strain energy of the $\{001\}_{fcc}$ orientation [30][34]–[36] .In addition, in some studies the relative density of defects between the two orientations is assumed to play a role [19][37]. To our knowledge, this is the first study reporting $\{111\}_{fcc}$ to $\{001\}_{fcc}$ transition in fcc epitaxial thin films on a c-sapphire substrate. A similar orientation relationship was observed for Al films on $\{111\}_{Si}$ and $\{111\}_{Ge}$ [1], but with a few differences. Firstly, the $\{001\}_{fcc}$ in Al grows at the lower deposition temperatures of 473- 553 K (0.51-0.59$T_m$ respectively). Secondly, in case of Al, the $\{001\}_{fcc}$ to $\{111\}_{fcc}$ transition occurs with increasing deposition temperature ($\{111\}_{fcc} \parallel \{111\}_{Si/Ge}$ occurs at > 598 K (0.64 $T_m$)) in contrast to CoCrFeNi on c-sapphire where the opposite trend is observed. Thirdly, in case of $\{001\}_{Al}$ on $\{111\}_{Si/Ge}$, the close-packed directions of the substrate and the film are parallel. In the present case these are at 45°.

#### 4.4.1 Thermodynamic factors related to OR1, OR2 and OR3

- ***Nanotwins in OR1 grains in contrast to micrometer twins in OR2 and OR3***

In the present study, the OR1 grains were heavily twinned (Fig. 8) in the as-deposited condition. The defect energy per unit volume considering nanotwins includes the energy of coherent $\Sigma 3/\{111\}_{fcc}$ twin boundaries (CTB) of area ~ $d^2$ (d is the diameter of the columnar grain) parallel to the substrate surface and that of incoherent $\Sigma 3/\{211\}_{fcc}$ twin boundary (ITB) segments[38][39] of area 'd*h' (h is the film thickness) along the columnar boundaries. The CTB energy per unit volume is given by $E_{CTB} = \gamma_{CTB} n_{CTB}/h$, where $\gamma_{CTB}$ is the CTB energy per unit area and $n_{CTB}$ is the number of coherent twin boundaries across the cross section. The CTB energy is expected to be close to half the SFE [40]. The SFE of the CoCrFeNi alloy is calculated to be ~ 30 mJ/$m^2$ [41], and is close to the experimental value for the quinary CoCrFeMnNi alloy [42]. Considering the CTB energy of ~15 mJ/$m^2$ and 100 CTBs across the

cross-section (h = 500 nm), the CTB energy per unit volume can be estimated as 3000 kJ/m$^3$. The ITB (columnar boundaries) energy per unit volume is given by $E_{ITB} = \frac{n_{ITB}\gamma_{ITB}}{d}$. The energy of incoherent segments for a fcc metal such as Cu could be a factor of 4 higher compared to the CTB energy [43]. Thus, we assume a $\gamma_{ITB} \approx 60$ mJ/m$^2$ for CoCrFeNi. Considering a grain size of 500 nm and approximating to hexagonal columns with 6 ITBs – each shared by two neighboring grains, $E_{ITB}$ per unit volume amounts to 360 kJ/m$^3$. The total twin boundary energy $E_{TB}$ per unit volume of $\{111\}_{fcc}$ grains amount to 3360 kJ/m$^3$.

The CTBs are observed in the cross sections of OR1 grains even at 1373 K with a spacing of hundreds of nanometers (Fig. 8 c,d). The CTB spacing in the OR3 grains is several micrometers (Fig. 7f, Figs. 2a, 4a). Similarly, cross-sections of OR2 grains showed single crystals without nanotwins (Fig. S8[11]). The OR1 grains contain a higher twin density, hence, a higher defect energy per unit volume.

- ***Anisotropy of elastic modulus favoring OR3***

The elastic strain energy can be calculated as $E_{strain} = \frac{1}{2} M_{\langle uvw \rangle} {\varepsilon_{thermal}}^2$, where $\varepsilon_{thermal} = (\alpha_{film} - \alpha_{substrate})\Delta T$ is the thermal strain in the system, $M_{\langle uvw \rangle}$ is the biaxial modulus of $\langle uvw \rangle$ direction, α is the thermal expansion coefficient, and ΔT is the temperature difference between the deposition temperature and annealing temperature. The thermal expansion coefficients for c-sapphire and CoCrFeNi alloy are $\alpha_{Al2O3} = [4.5 + 0.0062\,(T + 273) - 1.5 \times 10^{-6}(T + 273)^2]10^{-6}$/K [44]and $\alpha_{CoCrFeNi} = 1.73\,x10^{-5}[1 - exp(-T/158)]$ /K respectively [22]. The RT $M_{\{001\}}$ and $M_{\{111\}}$ were calculated (from the data available on CrMnFeCoNi single crystals[42]) as 172 GPa and 352 GPa. The elastic strain energy per m$^3$, for the $\{111\}_{fcc}$ is ~ 10,500 kJ/m$^3$ at 973 K. However, at temperatures greater than 573 K, the thin film relaxes its thermal stresses (Fig. 10). Hence, as a first approximation, the strain energy per unit volume stored in the system can be taken as the elastic strain energy at 573 K – that is ~ 2300 kJ/m$^3$ for the OR1. The strain energy for $\{001\}_{fcc}$ OR3 orientations is a factor of 2 lower with the absolute magnitude of 1100 kJ/m$^3$, a factor of two lesser.

- ***Relative values of epitaxial strains favoring OR2 and OR3 at higher temperatures***

The d-spacing of the close-packed direction in c-sapphire $\langle 30\bar{3}0 \rangle_{Al_2O_3}$ is 0.137 nm and that of $\langle 11\bar{2}0 \rangle_{Al_2O_3}$ is 0.238 nm. The epitaxial strain of OR1 considering lattice mismatch between $\langle 022 \rangle_{fcc}$ (d-spacing of 0.126 nm) and $\langle 30\bar{3}0 \rangle_{Al_2O_3}$ is isotropic with a tensile value of 0.09. For OR2, the lattice mismatch between $\langle 011 \rangle_{fcc}$ (0.252 nm) and $\langle 11\bar{2}0 \rangle_{Al_2O_3}$(0.238 nm) is isotropic and compressive with an epitaxial strain of 0.06. The $\langle 002 \rangle_{fcc}$ d-spacing of CoCrFeNi is 0.178 nm. In OR3 grains, alignment of one of the $\langle 002 \rangle_{fcc}$ directions along $\langle 30\bar{3}0 \rangle_{Al_2O_3}$ and the other at 90° along $\langle 11\bar{2}0 \rangle_{Al_2O_3}$ leads to linear strains of -0.28 and +0.34 respectively. Stresses in these films get increasingly compressive on annealing (Fig. 10). The compressive stress that develops on annealing is likely to promote OR2

(isotropic compressive epitaxial strain) and OR 3 (compressive epitaxial strains in one of the directions) over OR 1 (isotropic tensile epitaxial strain).

Although a mismatch of > 0.1 was typically considered an upper cutoff for the epitaxial film formation, many studies report epitaxy based on for $md_{substrate} = nd_{film}$. A well-known example is is Ag on Si [45] with a mismatch of -0.33, where epitaxy with a misfit dislocation every fourth Ag layer is observed. Hence large mismatches here could still lead to epitaxy with misfit dislocations at regular intervals.

Epitaxial strain energy depends on the temperature due to thermal expansion differences, and temperature dependence of the biaxial moduli. Further on the interface atomistic structure, for example interface reconstruction in $Ni/Al_2O_3$ [7] decreases the interfacial strain. Reported values are only true to the first approximation.

- ***Relative values of free surface and interfacial energies***

The $\{111\}_{fcc}$ grains including OR1 form due to a low value of free surface energy and the film-substrate interfacial energy. The surface energy of $\{111\}_{fcc}$ plane in CoCrFeNi alloy was calculated as 2.3 J/m$^2$[46]. Considering this value, the surface energy / unit volume of a film can be calculated as $E_{111} = \gamma_{111}/h$, that is 4,600 kJ/m$^3$, same order of magnitude as the strain and defect energies. The energy advantage of OR1 and OR2 over OR3 is likely to be reduced due to adsorption of gas molecules, further by the formation of oxide. Surface and interfacial energy values depend again on the local relaxation.

#### 4.4.2 Thermodynamic advantage of OR2, OR3 over OR1

The twin boundary energy of OR1 grains is of the same order of magnitude as the elastic strain energy, especially in the presence of a high density of growth twins – accounting to an advantage of ~ 3360 mJ/m$^3$ even at room temperature. The twin boundary energy is almost negligible in OR2 and OR3 grains – owing to the tens of micrometers twin spacing. The elastic strain energy is a factor of two lower for the OR 3 grains owing to a low modulus $\{001\}_{fcc}$orientation. Further, the unrelaxed epitaxial strain favors OR2 and OR3 at higher temperatures. Hence, thermodynamically OR2 and OR3 have an advantage over the OR1 grains at all temperatures. Note that the lower surface energy of OR1 or OR2 is less likely significant in films with thickness of 500 and 1000 nm.

#### 4.4.3 Nucleation advantage and metastability of OR 1

The OR1 grains form in as-deposited films due to their nucleation advantage and exhibit exceptional metastability up to 973 K due to kinetic reasons (Sec 4.1). At higher temperatures, the likely increase in twin spacing reduces the defect energy advantage of OR2 and OR3. But the strain energy advantage increases (more compressive stresses). The OR3 grains, greater than 100 nm appear with an area fraction of 0.03 at 973 K – only in 1 µm films, not in 500 nm films. Further the OR 1 fraction is almost negligible in the 1 µm thin films (with or without oxides) at 1223 K, but significant in the 500 nm films.

In 1 μm films, 0.91 – 0.96 of the area is covered by OR 3 + $\{345\}_{fcc}$. Both observations suggest that OR3 grains rapidly grow when kinetics is favorable.

#### 4.4.4 Oxide particles and kinetic factors

As explained in Sec. 4.3, grain growth of OR1 strongly depends on oxide layer and oxide particles, that of OR2 and OR3 are weakly dependent. Above 973 K, the OR1 grows rapidly in their presence, OR2 and OR3 in their absence. Notably, in all these ORs rapid grain growth starts at a temperature between 973 and 1223 K. Study of the related kinetic factor is beyond the scope of the current study.

The discussion above leads to a number of insights:

- The thermodynamic factors (defect and the strain energy) favor OR2 and OR3 over OR1 grains at all temperatures.
- The OR1 grains formed due to nucleation advantage remain metastable below 973 K (Sec. 4.3).
- The dominance of OR3 in thicker films, strongly indicate the role of strain energy in its appearance.
- The OR2 and OR3 grain boundary mobility is weakly dependent on the oxides, in contrast to OR1.

### 4.5. Twinning induced ORs

In addition to OR1, OR2 and OR3, six other ORs involving high index $\{hkl\}_{fcc}$ were identified in films deposited at 573 K and annealed above 973 K. The predominant was $\{345\}_{fcc} \parallel (0001)_{Al_2O_3}$. The $\{115\}_{fcc} \parallel (0001)_{Al_2O_3}$ and $\{221\}_{fcc} \parallel (0001)_{Al_2O_3}$ were observed in 500 nm film, encapsulated and annealed 1223 K, although with a miniscule area fraction (Table 1). The $\{447\}_{fcc} \parallel (0001)_{Al_2O_3}$, $\{146\}_{fcc} \parallel (0001)_{Al_2O_3}$ and $\{236\}_{fcc} \parallel (0001)_{Al_2O_3}$ were present in 1 μm films, annealed at 1223 K (consistently observed in multiple samples). These ORs grow with multiple variants, leading to many peaks in pole figures (Fig. 6,7, S6, S7). The low index directions $\langle 001\rangle_{fcc}$, $\langle 011\rangle_{fcc}$ and $\langle 111\rangle_{fcc}$ in many of these variants fall along the c-sapphire directions of the type $\langle 10\bar{1}l\rangle_{Al_2O_3}$ (located on the great circle containing A2 in Fig. 6c) and $\langle 11\bar{2}l\rangle_{Al_2O_3}$ (on the great circle containing A1 in Fig. 6c).

The $\{345\}_{fcc}$ accompanies OR3, in all 573 K deposited films with an exception of 500 nm films encapsulated and annealed at 1223 K. It occurs with a significant area fraction (0.35 – 0.42), a grain size of 2.0-3.5 μm in the 500 nm films and, 20 – 42 μm in the 1 μm films. Grain size is an order of magnitude larger compared to OR1- when co-existing. The $\{345\}_{fcc}$ grains (bluish) form the second predominant OR, only next to OR3 in 1 μm films annealed at 1223 K (and to a lesser extent in 500 nm films annealed at 1223, 1373 K without encapsulation). The $\{345\}_{fcc}$ OR is placed on the stereographic triangle, close to the $\{111\}_{fcc}$ corner, at an angular distance of 11.5° (Fig. 3, 5-7). The grains appear

to be twins in close to (but not exactly) $\{001\}_{fcc}$ grains (orange) (Fig. 6a). Notably, the $\{345\}_{fcc}$ is replaced by $\{115\}_{fcc}$ and $\{221\}_{fcc}$ in the 500 nm, encapsulated films – that did not contain oxides (Fig. 4). The $\{115\}_{fcc}$ and $\{221\}_{fcc}$ are well known twinned orientations of $\{111\}_{fcc}$ and $\{001\}_{fcc}$ respectively[47][48]. Hence, the primary and secondary twinning of close to $\{001\}_{fcc}$ and $\{111\}_{fcc}$ grains appears to be a possible explanation for the formation of high index orientations.

**4.5.1 ORs resulting from twinning in** $\{001\}_{fcc}$

The change in the A3 direction (the film normal direction) due to twinning of fcc crystals can be verified applying the twinning matrix in Ref.[49]. For the grains exactly oriented with OR3, primary twinning leads to $\{122\}_{fcc}$ [49]and secondary twins lead to $\{148\}_{fcc}$ and $\{447\}_{fcc}$ along the A3 axis.

The $\{345\}_{fcc}$ could form due to primary twinning of $\{017\}_{fcc}$ directions that are located at 8.1° angular distance from exact $\{001\}_{fcc}$ orientation. Similarly, the $\{146\}_{fcc}$ could occur due to primary twinning of $\{027\}_{fcc}$, that are at an angular distance of 16° from $\{001\}_{fcc}$.

**4.5.2 ORs resulting from twinning in** $\{111\}_{fcc}$

The primary twinning of $\{111\}_{fcc}$ orientations on the $\{111\}_{fcc}$ parallel to the film substrate interface leads to what is generally referred to as "OR1 twinned" or "OR2 twinned" orientations (Sec. 3.1.1,[3][5]). However, the twinning of $\{111\}_{fcc}$ grains on $\{111\}_{fcc}$ planes inclined to the film – substrate interface leads to $\{115\}_{fcc}$ type of orientation [47][48] observed in the 500 nm films without oxides. Further twinning of the $\{115\}_{fcc}$ orientation leads to $\{5\ 7\ 13\}_{fcc}$ among many others, that is 2.7° from the $\{236\}_{fcc}$, another OR observed in the study. Although the analysis for formation of high index ORs is preliminary, all these occur close to first or second order twinning of initial grain orientations within 16° from $\{001\}_{fcc}$ and $\{111\}_{fcc}$.

The quinary CoCrFeMnNi HEA in the bulk form has exhibited deformation by both dislocation plasticity[50][51] and twinning [52][53]. In thin metallic films on substrates, thermal stresses on annealing lead to extensive deformation by dislocation plasticity, twinning and diffusion creep [29][54]. In Au films deformation twinning occurs below a given film thickness [54]. In this study, all orientations related to twinning only occur in films where the $\{001\}_{fcc}$ and $\{111\}_{fcc}$ grain size is larger than 1 μm – that are likely to undergo plastic deformation due to thermal stresses. It appears that the deformation of large grains under thermal stresses lead to twinning – that forms these unique ORs. The low stacking fault energy of the alloy under study [55] makes twinning a likely mechanism. Constraint to deformation due to the thin film dimensions and surface oxide, that suppresses dislocation activity is also likely to be a factor. These hypotheses lead the authors towards systematic studies in alloy thin film systems of various compositions in the future.

## 5. Summary and Conclusions

CoCrFeNi alloy thin films sputter deposited on a single crystal c-sapphire or $(0001)_{Al_2O_3}$ form specific ORs in as deposited and annealed state, many of which are reported for the first time.

- Films deposited at RT and 573 K on c-sapphire formed predominantly OR1 heteroepitaxy with $\{111\}_{fcc}||(0001)_{Al_2O_3}\ \langle 110\rangle_{fcc}||\langle 10\bar{1}0\rangle_{Al_2O_3}$.
- The OR1 grains exhibit a highly defective structure containing nanotwins in the cross section, nanopores at triple junctions, oxide surface layer and the fine oxides formed on annealing – that lead to an exceptional stability of the grain size at least up to 973 K (0.56 $T_m$).
- A new orientation relationship formed in films deposited at 573 K on annealing at 1223 and 1373 K, ("OR 3") – with $\{001\}_{fcc}||(0001)_{Al_2O_3}\ \langle 100\rangle_{fcc}||\langle 10\bar{1}0\rangle_{Al_2O_3}$. In addition, OR2 $\{111\}_{fcc}||(0001)_{Al_2O_3}\ \langle 110\rangle_{fcc}||\langle 11\bar{2}0\rangle_{Al_2O_3}$ occurred in a small area fraction in some films.
- Analysis indicated the thermodynamic growth advantage for OR2 and OR3 grains over OR1 at all temperatures. However, kinetic barriers stop their growth up to 973 K (0.56 $T_m$).
- Above this temperature, grain growth behavior of different ORs is strongly dependent on oxides. Absence of oxides strongly promotes the growth of OR1 over OR2 and OR3. In the presence of oxides, OR1 remains stable in grain size and gets consumed by rapidly growing OR2 and OR3. The OR3 almost eliminates OR1 in thicker films (1 µm), indicating the role of strain energy in its growth.
- The study reports an unusual OR with $\{345\}_{fcc} \parallel (0001)_{Al_2O_3}$, in area fraction of 0.3-0.5. This occurs in addition to OR1, OR2 and OR3, in films deposited at 573 K, annealed at 1223 K. The OR is related to twinning in close to $\{001\}_{fcc}$ grains.
- Similarly, $\{115\}_{fcc}$, $\{221\}_{fcc}$ and $\{447\}_{fcc}$ related to twinning of $\{001\}_{fcc}$ and $\{111\}_{fcc}$ occur in selected annealed films. In addition, $\{146\}_{fcc}$ and $\{236\}_{fcc}$ that are presumably related to primary and secondary twinning in $\{001\}_{fcc}$ and $\{111\}_{fcc}$ grains also occur consistently in the 1 µm films. The deformation under thermal stresses, constraint to dislocation plasticity and a high twinning propensity of the alloy are possible reasons for the formation of these high index $\{hkl\}_{fcc}$ ORs.

**Acknowledgements:**

The study was carried out under the DFG-ANR collaborative project ‘‘Analysis of the stability of High Entropy Alloys by Dewetting of thin films’’ under the grant LU1175/22-1 (RU Bochum), DE796/11-1 (MPIE) and ANR-AHEAD-16-CE92-0015-01 (CINaM). Authors gratefully acknowledge Prof. Paul Wynblatt (Carnegie Mellon University, Pittsburgh, USA) for useful discussions. Occasional discussions with C. Kirchlechner and C. Liebscher, assistance with Ar ion polishing by M.J. Duarte, and S. Nandy in the initial phase of the project, technical assistance by M. Nellessen, and K. Angenendt are acknowledged. Annealing at 1373 K was carried out with the help of J. Wichert.

MK Kini gratefully acknowledges Prof. Vikram Jayaram (Indian Institute of Science, Bangalore) for discussions on crystallography and stereographic projections back in 2008, that were critical in analyzing the results. Further, she acknowledges Prof. Indradev Samajdar and Aditya Prakash (Indian Institute of Technology, Bombay) for access to TSL OIM data analysis software during manuscript preparation.

**Figures with captions**

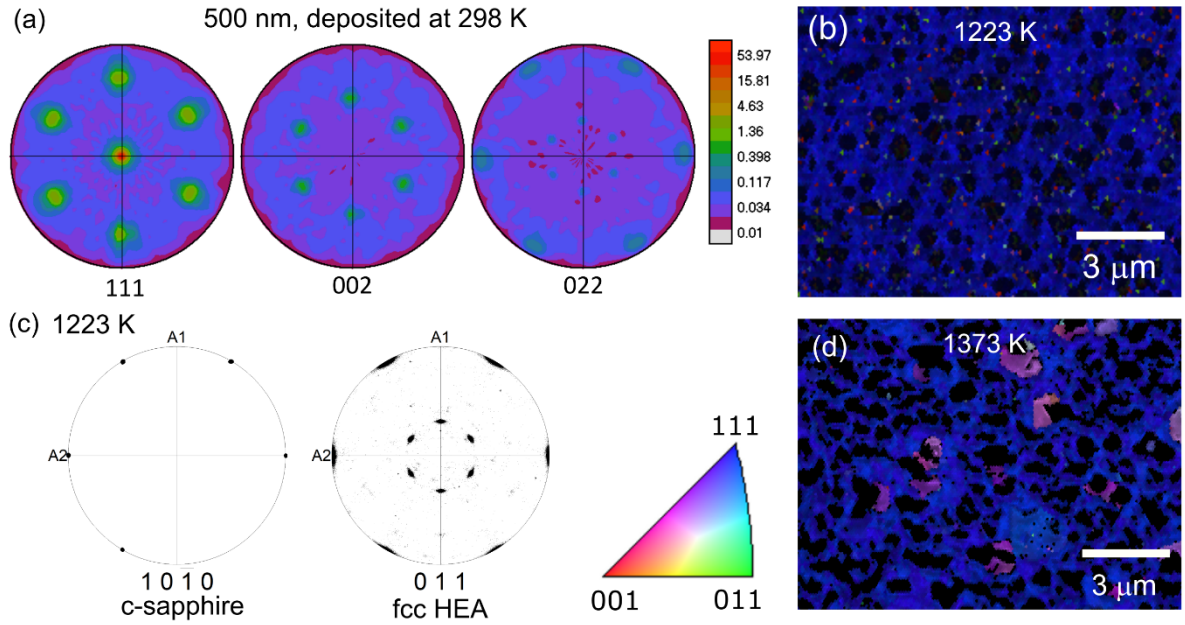


Fig 1: XRD and EBSD data of 500 nm thick CoCrFeNi films on c-sapphire deposited at RT. (a) X-ray pole figures of as-deposited film; (b, d) are EBSD IPF maps (along A3 – the substrate normal) of films annealed at 1223 K (0.71 $T_m$) and 1373 K (0.79 $T_m$), respectively. IPFs imply $\{111\}_{fcc}||(0001)_{Al_2O_3}$. (c) typical pole figures of fcc HEA and c-sapphire of an annealed sample (here, 1373 K) that imply $\langle 011\rangle_{fcc}||\langle 10\bar{1}0\rangle_{Al_2O_3}$. Black areas in (b, d) correspond to pores formed during dewetting.

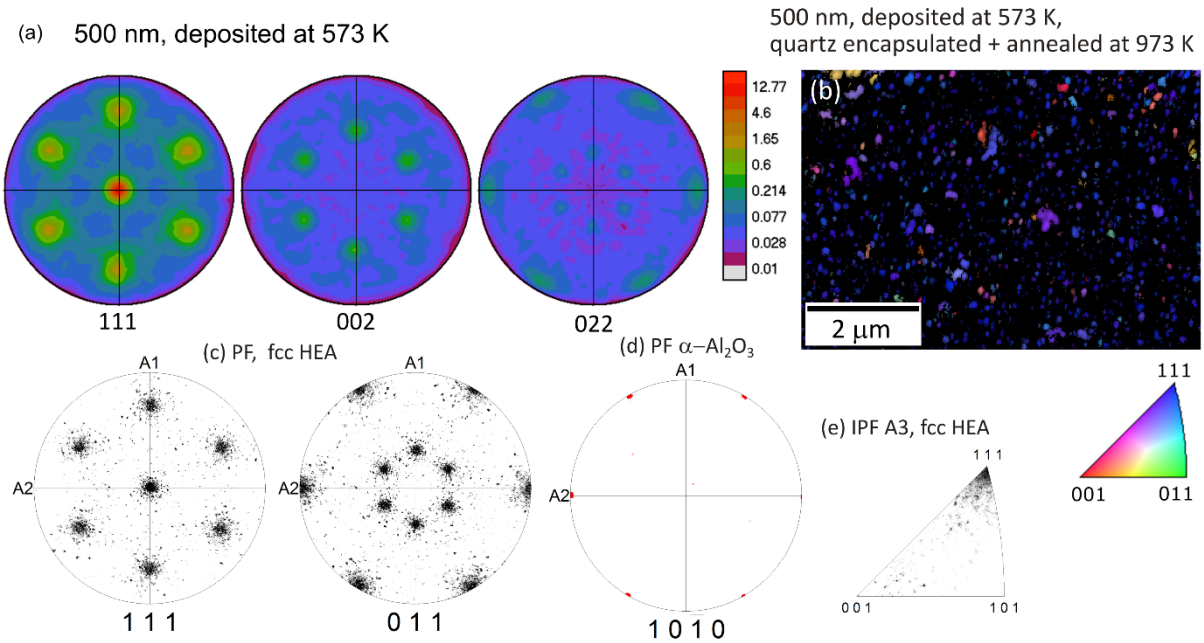


Fig 2: XRD and EBSD data for a CoCrFeNi 500nm thick film deposited at 573 K on c-sapphire. (a) X-ray pole figures of as-deposited film, (b-d) are for a film quartz encapsulated and annealed at 973 K for 2 hours. (b) IPF map along A3 (normal direction) indicating only the grains larger than 100 nm (resolution limit of EBSD technique), and (c,d) PFs for the films and the substrate indicating that the identified grains are predominantly OR1 type. (e) IPF along A3.

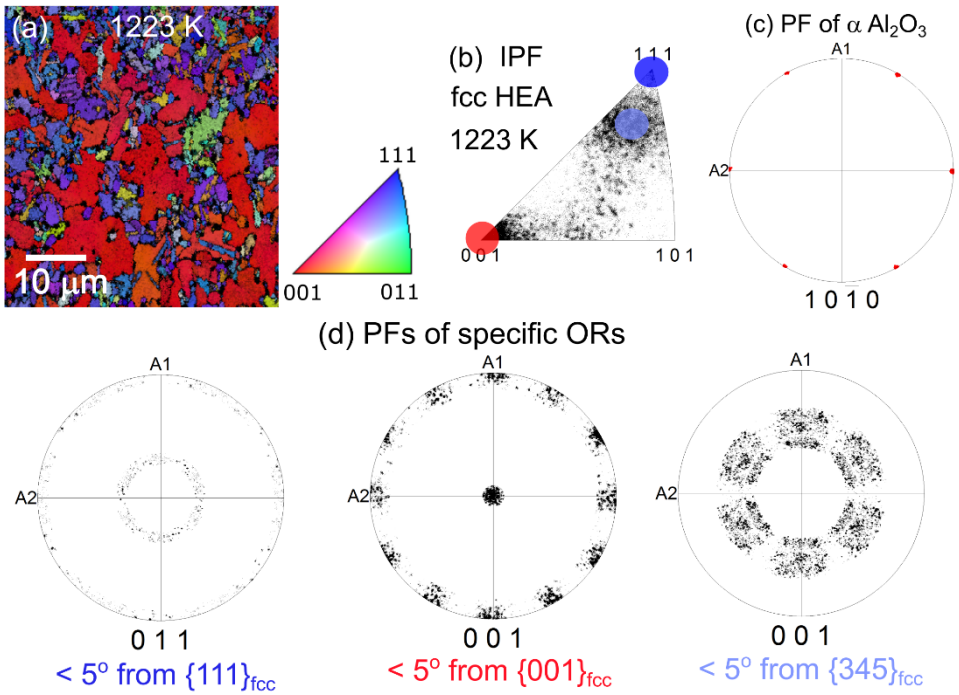


Fig 3: EBSD data of a CoCrFeNi 500nm thick film deposited at 573 K on c-sapphire, annealed at 1223 K. (a) IPF map along A3 (normal direction), (b) IPF along A3 highlighting dominant ORs. (c,d) PF of c-sapphire compared to the PFs of fcc data partitioned into three dominant ORs: $\{111\}_{fcc}$ fiber (dark blue dot in (b)), OR3 (red dot in (b)) and $\{345\}_{fcc}||(0001)_{Al_2O_3}$(light blue dot in (b)).

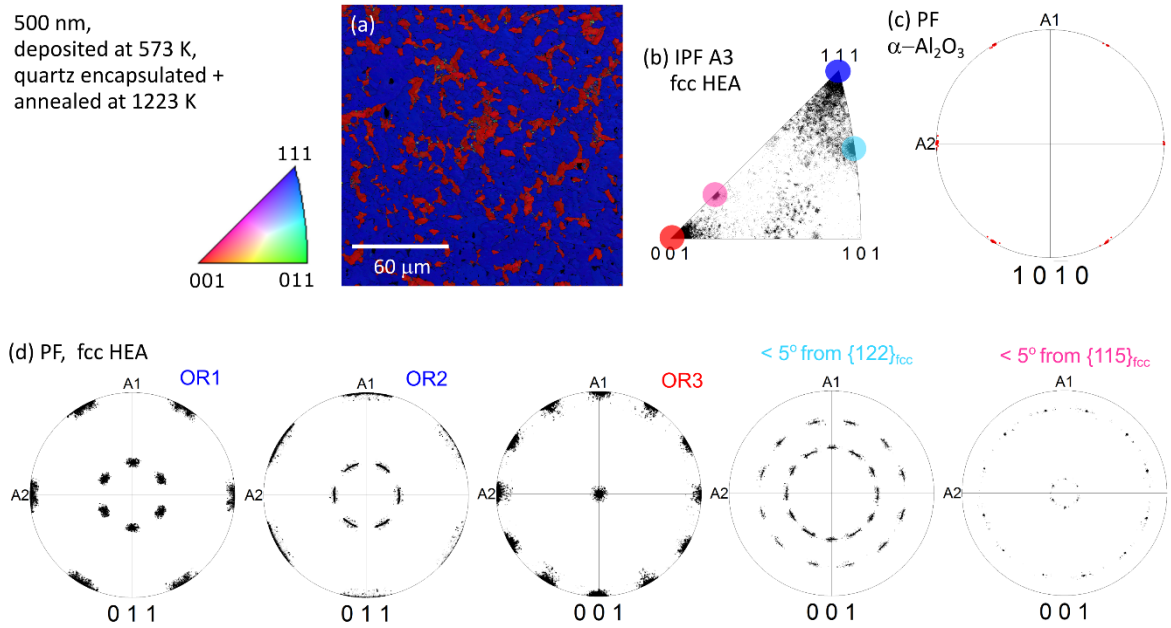


Fig. 4: Results on a 500 nm thin film of CoCrFeNi deposited at 573 K on c-sapphire, quartz encapsulated and annealed at 1223 K for 2 hours. (a) EBSD IPF map of the entire region along A3, (b) IPF along A3, highlighting five dominant ORs, (c) PF of the sapphire substrate and (d) PFs of the fcc film partitioned into specific ORs: OR1 and OR2 (dark blue dot in (b)), OR3 (red dot), $\{122\}_{fcc}$ (light blue dot) and $\{115\}_{fcc}$ (pink dot).

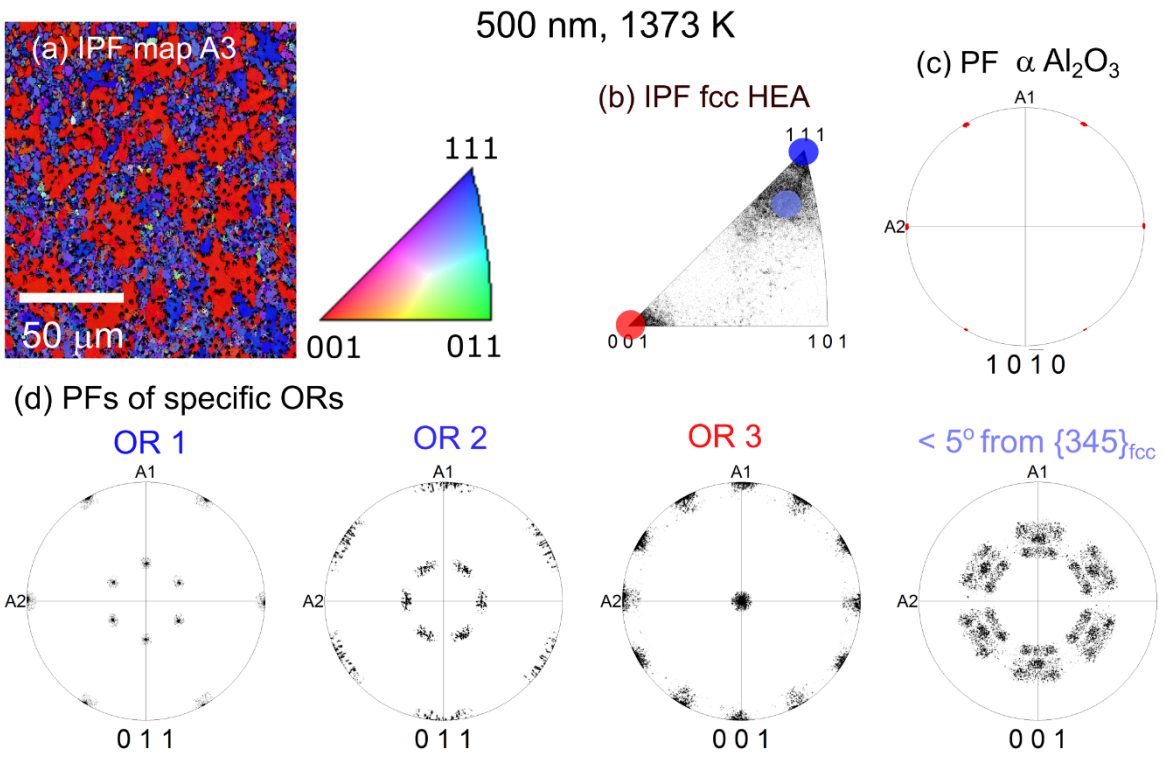


Fig 5: Results on CoCrFeNi 500 nm film on c-sapphire deposited at 573 K and annealed at 1373 K. (a) IPF map along A3, (b) IPF highlighting predominant ORs, (c) PF of c-sapphire compared to (d) PFs of the data partitioned into dominant ORs: OR1 and OR2 (both are included in the dark blue dot in (b)), OR3 (red dot in (b)) and $\{345\}_{fcc}||(0001)_{Al_2O_3}$(light blue dot in (b)).

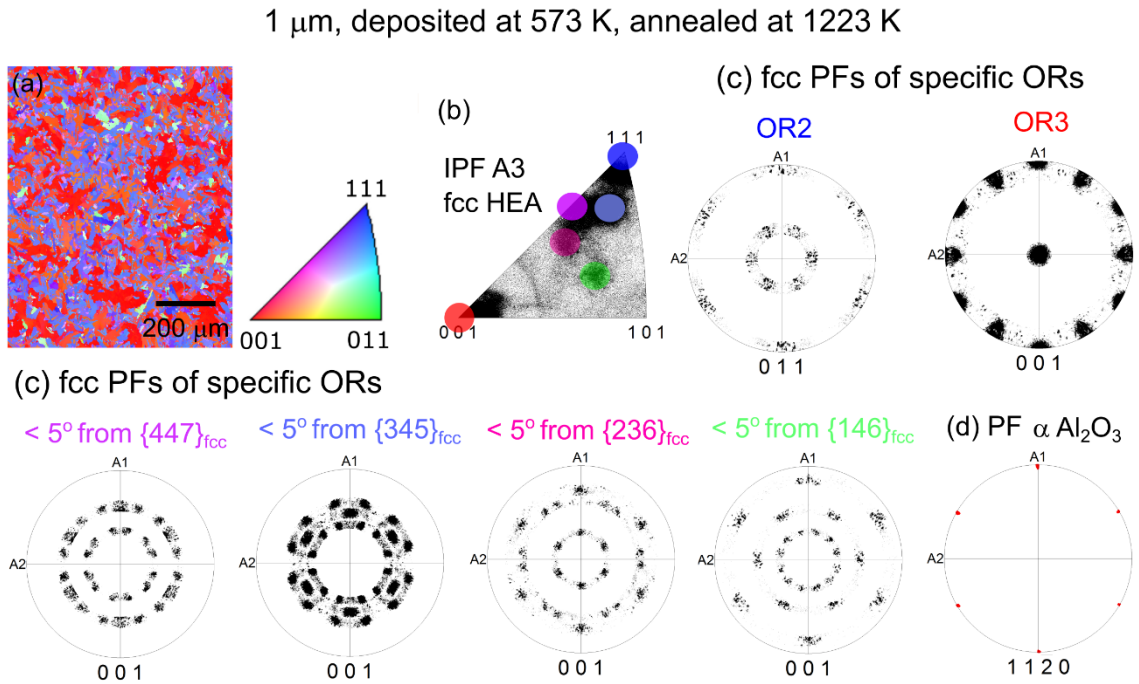


Fig 6: Results on a 1 μm thin film of CoCrFeNi deposited at 573 K on c-sapphire and annealed at 1223 K for 2 hours. (a) EBSD IPF map of the entire region along A3, (b) IPF along A3, highlighting 6 dominant ORs, (c) PFs of the fcc film partitioned into specific ORs: OR2 (dark blue dot in (b)), OR3 (red dot), $\{447\}_{fcc}$ (purple dot), $\{345\}_{fcc}$ (light blue dot), $\{236\}_{fcc}$ (pink dot) and $\{146\}_{fcc}$ (green dot), (d) PF of the sapphire substrate.

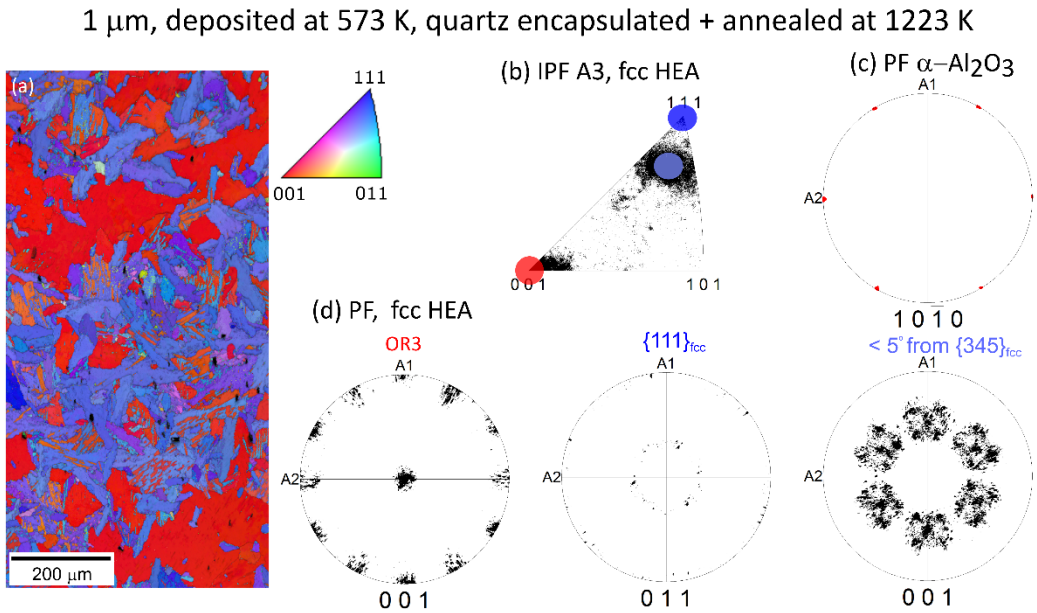


Fig 7: Results on a 1 μm thin film of CoCrFeNi deposited at 573 K on c-sapphire, quartz encapsulated and annealed at 1223 K for 2 hours. (a) EBSD IPF map of the entire region along A3, (b) IPF along A3, highlighting three dominant ORs, (c) PF of the sapphire substrate and (d) PFs of the fcc film partitioned into specific ORs: OR3 (red dot), $\{111\}_{fcc}$ (dark blue dot in (b)) and $\{345\}_{fcc}$ (light blue dot). The $\{236\}_{fcc}$ and $\{146\}_{fcc}$ are also present in miniscule amounts (not shown).

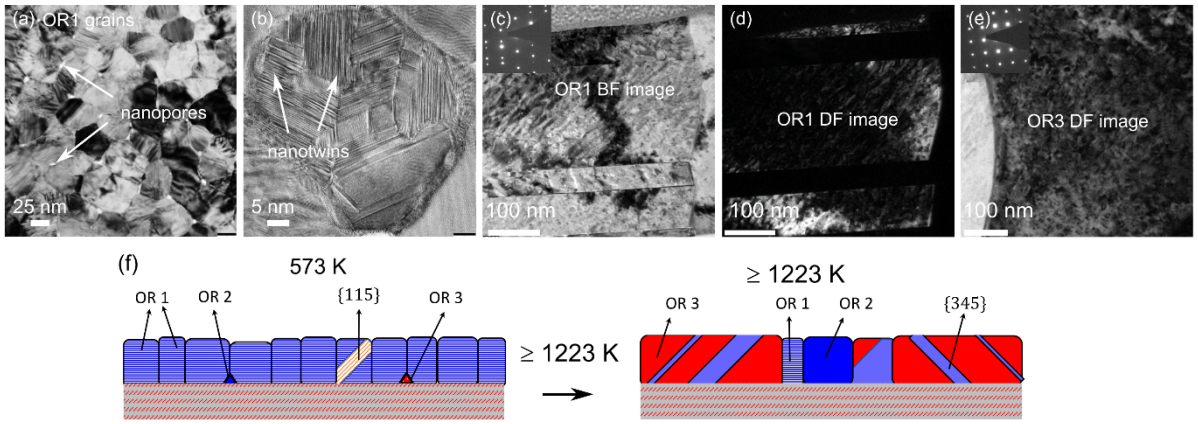


Fig 8: Coherent twin boundaries and nanopores in TEM images (a-f). (a) Plan-view TEM image of a 500 nm film on c-sapphire deposited at 573 K displaying nanopores at triple junctions. (b) Plan-view TEM image of a 1 µm film, deposited at 573 K with a complex nanotwinned structure of $\{111\}$ oriented grains. (c) and (d) are TEM bright field and corresponding dark field images of an OR1 grain in a 500 nm film, deposited at 573 K and annealed at 1373 K, (e) is the dark field image of an OR3 grain in the same film. Insets of figures (c) and (e) are selected area diffraction patterns (SADP) in $\langle 110 \rangle$ and $\langle 100 \rangle$ zone axes, respectively. The $\langle 110 \rangle$ SADP displays twin reflections. (f) is the schematic of the grain structure of a c-sapphire film after deposition at 573 K, and subsequent microstructure evolution after a 2h anneal at T ≥ 1223K.

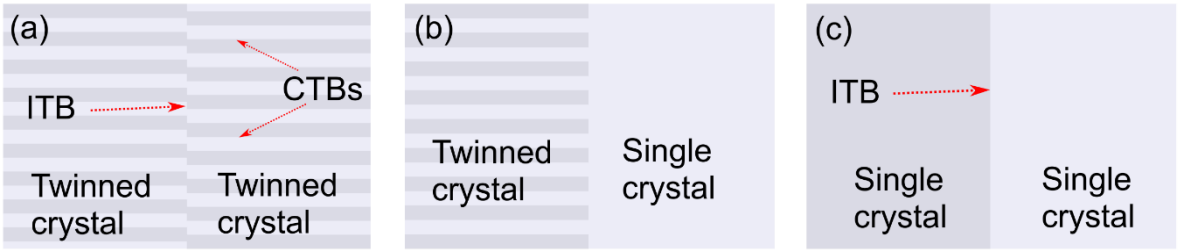


Fig. 9: Schematic of suggested configurations of (a) two twinned crystals, (b) single crystal – nanotwinned crystal and (c) two single crystals with same orientations as the parent crystal in (a) and (b) to compare ITB mobility in nanotwinned crystals compared to that in single crystals.

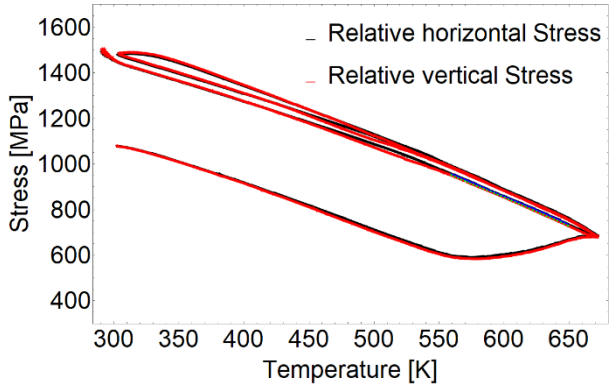


Fig. 10: Thermal stresses in films on c-sapphire – relaxing at a value of ~ 600 MPa at temperatures > 573 K.

**References**


[1] K.H. Westmacott, S. Hinderberger, U. Dahmen, *Philosophical Magazine A* **2001**, *81*, 1547.
[2] Pashley DW, *Adv Phys* **1965**, *14*, 327.
[3] G. Dehm, H. Edongue, T. Wagner, S.H. Oh, E. Arzt, *ZEITSCHRIFT FUR METALLKUNDE*, **1995**, *96*, 249.
[4] G. Dehm, B.J. Inkson, T. Wagner, *Acta Mater* **2002**, *50*, 5021.
[5] S.W. Hieke, B. Breitbach, G. Dehm, C. Scheu, *Acta Mater* **2017**, *133*, 356.
[6] G. Dehm, C. Scheu, M. Rühle, R. Raj, *Acta Mater* **1998**, *46*, 759.
[7] H. Meltzman, D. Mordehai, W.D. Kaplan, *Acta Mater* **2012**, *60*, 4359.
[8] A.A. Taylor, S.H. Oh, G. Dehm, *J Mater Sci* **2010**, *45*, 3874.
[9] D. Amram, E. Rabkin, *Acta Mater* **2013**, *61*, 4113.
[10] S. Ramanathan, B.M. Clemens, P.C. McIntyre, U. Dahmen, *Philosophical Magazine A* **2001**, *81*, 2073.
[11] Y. Addab, M.K. Kini, B. Courtois, A. Savan, A. Ludwig, N. Bozzolo, C. Scheu, G. Dehm, D. Chatain, *Acta Mater* **2020**, *200*, 908.
[12] D.L. Miller, M.W. Keller, J.M. Shaw, K.P. Rice, R.R. Keller, K.M. Diederichsen, *AIP Adv* **2013**, *3*, 082105.
[13] S. Curiotto, H. Chien, H. Meltzman, P. Wynblatt, G.S. Rohrer, W.D. Kaplan, D. Chatain, *Acta Mater* **2011**, *59*, 5320.
[14] O. Anderoglu, A. Misra, H. Wang, F. Ronning, M.F. Hundley, X. Zhang, *Appl Phys Lett* **2008**, *93*, 083108.
[15] D. Bufford, H. Wang, X. Zhang, *Acta Mater* **2011**, *59*, 93.
[16] N.M. Heckman, L. Velasco, A.M. Hodge, *MRS Commun* **2017**, *7*, 253.
[17] G.-D. Sim, J.A. Krogstad, K.Y. Xie, S. Dasgupta, G.M. Valentino, T.P. Weihs, K.J. Hemker, *Acta Mater* **2018**, *144*, 216.
[18] N. Chawake, J. Zálešák, C. Gammer, R. Franz, M.J. Cordill, J.T. Kim, J. Eckert, *Scr Mater* **2020**, *177*, 22.
[19] E.A. Ellis, M. Chmielus, M.-T. Lin, H. Joress, K. Visser, A. Woll, R.P. Vinci, W.L. Brown, S.P. Baker, *Acta Mater* **2016**, *105*, 495.
[20] N. Thangaraj, K.H. Westmacott, U. Dahmen, *Appl Phys Lett* **1992**, *61*, 913.
[21] S. Lee, D. Chatain, C.H. Liebscher, G. Dehm, *Scr Mater* **2021**, *203*, 114044.
[22] G. Laplanche, P. Gadaud, C. Bärsch, K. Demtröder, C. Reinhart, J. Schreuer, E.P. George, *J Alloys Compd* **2018**, *746*, 244.
[23] M.G. Emigh, R.D. McAuliffe, C. Chen, J.C. Mabon, T. Weihs, K.J. Hemker, D.P. Shoemaker, J.A. Krogstad, *Acta Mater* **2018**, *156*, 411.
[24] N. Bernstein, E.B. Tadmor, *Phys Rev B* **2004**, *69*, 094116.
[25] R. Berlia, J. Rajagopalan, *Scr Mater* **2022**, *213*, 114594.
[26] F. Duan, Y. Lin, J. Pan, L. Zhao, Q. Guo, D. Zhang, Y. Li, *Sci Adv* **2024**, *7*, eabg5113.
[27] Q. Li, S. Xue, P. Price, X. Sun, J. Ding, Z. Shang, Z. Fan, H. Wang, Y. Zhang, Y. Chen, H. Wang, K. Hattar, X. Zhang, *Nanoscale* **2020**, *12*, 1356.
[28] E. Nes, N. Ryum, O. Hunderi, *Acta Metallurgica* **1985**, *33*, 11.
[29] D. Weiss, H. Gao, E. Arzt, *Acta Mater* **2001**, *49*, 2395.
[30] Carl.V. Thompson, R. Carel, *Materials Science and Engineering: B* **1995**, *32*, 211.
[31] R. Carel, C. V Thompson, H.J. Frost, *Acta Mater* **1996**, *44*, 2479.
[32] S.P. Baker, A. Kretschmann, E. Arzt, *Acta Mater* **2001**, *49*.
[33] P. Sonnweber-Ribic, P. Gruber, G. Dehm, E. Arzt, *Acta Mater* **2006**, *54*, 3863.
[34] C. V Thompson, *Annual Review of Materials Science* **2000**, *30*, 159.
[35] C. V Thompson, R. Carel, *J Mech Phys Solids* **1996**, *44*, 657.
[36] R.C. Cammarata, *Prog Surf Sci* **1994**, *46*, 1.
[37] S.P. Baker, B. Hoffman, L. Timian, A. Silvernail, E.A. Ellis, *Acta Mater* **2013**, *61*, 7121.

[38] J. Wang, N. Li, O. Anderoglu, X. Zhang, A. Misra, J.Y. Huang, J.P. Hirth, *Acta Mater* **2010**, *58*, 2262.
[39] S. Ahmad, T. Brink, C.H. Liebscher, G. Dehm, *Acta Mater* **2023**, *243*, 118499.
[40] M. Chassagne, M. Legros, D. Rodney, *Acta Mater* **2011**, *59*, 1456.
[41] A.J. Zaddach, C. Niu, C.C. Koch, D.L. Irving, *JOM* **2013**, *65*, 1780.
[42] N.L. Okamoto, S. Fujimoto, Y. Kambara, M. Kawamura, Z.M.T. Chen, H. Matsunoshita, K. Tanaka, H. Inui, E.P. George, *Sci Rep* **2016**, *6*, 35863.
[43] B. Straumal, Y. Kucherinenko, B. Baretzky, Rev Adv Mater Sc, **2004**, 7, 23
[44] L. Ben Freund, S. Suresh, *Thin Film Materials: Stress, Defect Formation and Surface Evolution*, Cambridge University Press**2004**.
[45] F.K. LeGoues, M. Liehr, M. Renier, W. Krakow, *Philosophical Magazine B* **1988**, *57*, 179.
[46] X. Zhou, W.A. Curtin, *Acta Mater* **2020**, *200*, 932.
[47] G. Gottstein, *Acta Metallurgica* **1984**, *32*, 1117.
[48] S. Mahajan, G.Y. Chin, *Acta Metallurgica* **1973**, *21*, 173.
[49] K.W. Andrews, W. Johnson, *British Journal of Applied Physics* **1955**, *6*, 92.
[50] R. Raghavan, C. Kirchlechner, B.N. Jaya, M. Feuerbacher, G. Dehm, *Scr Mater* **2017**, *129*, 52.
[51] S. Lee, M.J. Duarte, M. Feuerbacher, R. Soler, C. Kirchlechner, C.H. Liebscher, S.H. Oh, G. Dehm, *Mater Res Lett* **2020**, *8*, 216.
[52] G. Laplanche, A. Kostka, O.M. Horst, G. Eggeler, E.P. George, *Acta Mater* **2016**, *118*, 152.
[53] K.V.S. Thurston, A. Hohenwarter, G. Laplanche, E.P. George, B. Gludovatz, R.O. Ritchie, *Intermetallics (Barking)* **2019**, *110*, 106469.
[54] G. Dehm, S.H. Oh, P. Gruber, M. Legros, F.D. Fischer, *Acta Mater* **2007**, *55*, 6659.
[55] S. Zhao, G.M. Stocks, Y. Zhang, *Acta Mater* **2017**, *134*, 334.

Table 1: Deposition, annealing conditions, texture and grain size of all films in the study. Note: (a) Area fraction of ORs do not always add up to 1. This is due to a combination of unidentified orientations and pores formed due to dewetting. (b) Error bars in grain size correspond to the first standard deviation.
* The orientation relationship is either OR1 or OR1 – twinned. A double Kikuchi pattern is observed. Individual pattern from either variant of OR1 cannot be distinguished. Hence grain size is not reported.

| **Deposition temperature (K)** | **Annealing temperature (K), time (h)** | **Film Thickness (nm)** | **ORs / Heteroepitaxy** | **Grain size (nm or µm)** | **Area fraction of components / ORs** |
|---|---|---|---|---|---|
| 298, annealed at 573 K for 12 hours | - | 500 | OR1 | (36 ± 22) nm (SEM) | unavailable |
| | 973, 2 | | OR1 | unreliable* | 1.0 |
| | 1223, 2 | | OR1 | (780 ± 480) nm | 1.0 |
| | 1373, 2 | | OR1, $\{447\}_{fcc}$ | (8.5 ± 5.0) µm (Overall grain size) | 0.61 (OR1), 0.05 $\{447\}_{fcc}$ |
| 573 | - | 500 | OR1 | (48 ± 35) nm (SEM) | unavailable |
| | 973, 2 | | OR1, OR3 | Unreliable* | OR3 < 0.05 |
| | Quartz encapsulated, 973, 2 | | OR1 | < 100 nm | unavailable |
| | 1223, 2 | | $\{111\}_{fcc}$ OR3, $\{345\}_{fcc}$ | (1.5 ± 1.0) µm $\{111\}_{fcc}$, (6.0 ± 3.3) µm (OR3), (2.0 ± 1.2) µm $\{345\}_{fcc}$ | 0.01$\{111\}_{fcc}$, 0.40 (OR3), 0.38 $\{345\}_{fcc}$ |
| | Quartz encapsulated, 1223 K, 2 | | OR1, OR2, OR3, | (23 ± 13) µm (OR1), (1.3 ± 1.3) µm (OR2), (5.0 ± 2.2) µm (OR3), (0.46 ± 0.21) µm $\{122\}_{fcc}$ | 0.78 (OR1) 0.01 (OR2) 0.18 (OR3) 0.004 $\{122\}_{fcc}$ |

| | | | | | |
|---|---|---|---|---|---|
| | | | $\{122\}_{fcc}$, $\{115\}_{fcc}$ | (0.40 ± 0.17) µm $\{115\}_{fcc}$ | 0.001 $\{115\}_{fcc}$ |
| | 1373, 2 | | OR1, OR2, OR3, $\{345\}_{fcc}$ | (2.3 ± 1.0) µm (OR1), (7.3 ± 2.8) µm (OR2), (14 ± 8.5) µm (OR3), (3.5 ± 2.3) µm $\{345\}_{fcc}$ | 0.02 (OR1), 0.06 (OR2), 0.42 (OR3), 0.41 $\{345\}_{fcc}$ |
| 573 | - | 1000 | Predominantly OR 1 | (60 – 100) nm | - |
| | 973, 2 | | Predominantly OR 1 + some OR 3 | (600 ± 450) nm (overall grain size) | 0.58 (OR1), 0.03 (OR3) |
| | 1223, 2 | | OR2, OR3, $\{345\}_{fcc}$, $\{447\}_{fcc}$, $\{146\}_{fcc}$, $\{236\}_{fcc}$, | (18 ± 12) µm (OR2), (46 ± 31) µm (OR3), (20 ± 11) µm $\{345\}_{fcc}$, (13 ± 6) µm $\{447\}_{fcc}$, (19 ± 10) µm $\{146\}_{fcc}$, (10 ± 5) µm $\{236\}_{fcc}$ | 0.01 (OR2), 0.56 (OR3), 0.35 $\{345\}_{fcc}$, 0.04 $\{447\}_{fcc}$, 0.02 $\{146\}_{fcc}$, 0.02 $\{236\}_{fcc}$ |
| | Quartz encapsulated, 1223, 2 | | $\{111\}_{fcc}$, OR3, $\{345\}_{fcc}$ $\{146\}_{fcc}, \{236\}_{fcc}$ | Insufficient data $\{111\}_{fcc}$ (140 ± 100) nm (OR3) (42 ± 26) nm $\{345\}_{fcc}$ Insufficient data for $\{146\}_{fcc}, \{236\}_{fcc}$ | < 0.01, $\{111\}_{fcc}$, 0.53 (OR3) 0.43 $\{345\}_{fcc}$ < 0.01, $\{146\}_{fcc}, \{236\}_{fcc}$ |